CRYSTAL GROWTH & DESIGN
pubs.acs.org/crystal
Article

Nucleation of Threading Dislocations in 4H-SiC at Early Physical-Vapor-Transport Growth Stage

Qinqin Shao,[#] Wenhao Geng,[#] Suocheng Xu, Penglei Chen, Xi Zhang, Ruohan Shen, He Tian, Xiaodong Pi,* Deren Yang, and Rong Wang*

Cite This: *Cryst. Growth Des.* 2023, 23, 5204−5210

Read Online

ACCESS | Metrics & More | Article Recommendations

ABSTRACT: In this work, we identify the nucleation mechanism of threading dislocations (TDs) associated with stacking faults (SFs) and 15R-SiC at the early growth stage of 4H-SiC single crystals grown by the physical vapor transport (PVT) technology. By combining molten KOH etching and photochemical etching, we successfully reveal etch pits of TDs and linear etch patterns of SFs on the (11$\bar{2}$0) surface of 4H-SiC single crystals. Systematic investigations based on transmission electron microscopy (TEM) observations and Raman analysis indicate that the Si−C bilayer stacking sequence of SFs is (3, 2) in Zhdanov's notation. The accumulation of SFs (3, 2) gives rise to the polymorph fluctuation and thus the formation of 15R-SiC at the early PVT growth stage of 4H-SiC single crystals. Quantitative stress analyses indicate that the strain field distributions along the SFs (3, 2) and the 15R-/4H-SiC interfaces are inhomogeneous, which give rise to the nucleation of TDs and low-angle grain boundaries (LAGBs), respectively. The nucleation of LAGBs releases the high stress at the 15R-/4H-SiC interface, which facilities the following 4H-SiC single-crystal growth. Our work indicates that the avoidance of polymorph fluctuation is important to the reduction of TDs at the early growth stage of PVT-grown 4H-SiC single crystals.

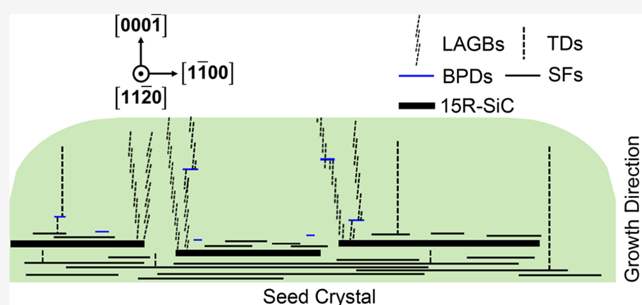

Downloaded via XIAMEN UNIV on April 11, 2024 at 12:17:54 (UTC).
See https://pubs.acs.org/sharingguidelines for options on how to legitimately share published articles.

1. INTRODUCTION

The wide band gap, high electric breakdown field, high electron mobility, and high thermal conductivity of 4H silicon carbide (4H-SiC) have positioned it as the leading candidate in high-power and high-frequency electronics.[1−5] Although 4H-SiC has been successfully used in the applications, such as electronic vehicles and power transmission systems, the high-density dislocations still pose severe degradation on the performance of 4H-SiC-based devices.[6−8] Threading screw dislocations (TSDs) and threading edge dislocations (TEDs) have been found to reduce the carrier lifetime and increase the leakage current of power devices based on 4H-SiC.[9−12] Meanwhile, basal plane dislocations (BPDs) have been identified as the origin of the expansion of a single Shockley stacking fault, which is responsible for bipolar degradation.[4,13] The detrimental effect of BPDs can be relieved by promoting the transition from BPDs to TEDs during the homoepitaxy of 4H-SiC.[14,15] However, over 95% threading dislocations (TDs) are replicated from 4H-SiC substrates to 4H-SiC epitaxial films, which pushes forward a great demand to reduce the density of TDs in 4H-SiC substrates.

During the physical-vapor-transport (PVT) growth of 4H-SiC single crystals, TDs are formed under the thermal stress induced by the temperature gradient, as well as the misfit stress introduced by secondary precipitates, two-dimensional islands, polymorphs, and inclusions.[3,16,17] Synchrotron X-ray topography (XRT) observations demonstrate that most TDs are generated at the initial stage of crystal growth as a result of growth condition discontinuities, such as temperature profile, C/Si ratio, and doping concentrations.[18,19] TDs are also found to replicate from TDs in the seed crystal.[3] Furthermore, the conversion from other kinds of defects to TDs is another important generation source of TDs during the single-crystal growth of 4H-SiC. Several TSDs can be generated from the dissociation of micropipes.[20,21] TSDs and TEDs can be formed by the conversion from stacking faults and BPDs, respectively.[22−27]

In this work, the generation mechanism of TDs originated from stacking faults (SFs) and polymorph fluctuation-induced 15R-SiC at the early stage of the PVT growth of 4H-SiC single crystals is proposed by comprehensive defect-selective chemical etching and detailed microstructure analyses. By combining molten KOH etching and photochemical etching

Received: April 6, 2023
Revised: May 19, 2023
Published: June 5, 2023

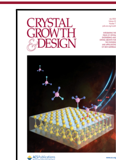

© 2023 American Chemical Society

https://doi.org/10.1021/acs.cgd.3c00416
Cryst. Growth Des. 2023, 23, 5204−5210

on the $(11\bar{2}0)$ surface of 4H-SiC, we successfully reveal TD-related pits located at linear etch patterns related to SF (3, 2), as well as low-angle grain boundary (LAGB)-related etched lines at the interface between 15R-SiC and 4H-SiC. Detailed geometric phase analysis (GPA) indicates that the strain field distribution along the SF (3, 2) is inhomogeneous, which gives rise to the formation of TDs located at SFs (3, 2). As the PVT growth proceeds, the accumulation of high density of SFs (3, 2) gives rise to the polymorph fluctuation and thus the formation of 15R-SiC. Similarly, we find that the strain field along the interface between 15R-SiC and 4H-SiC is also inhomogeneous, which initiates the formation of LAGBs. Furthermore, we find that the LAGBs in 4H-SiC are capable of being kinked by the interaction between the TEDs constituting the LAGB and a BPD.

2. EXPERIMENTAL METHODS

2.1. Single-Crystal Growth and Revelation of Defects in 4H-SiC. 4H-SiC single crystals used in this work were grown by the PVT technique on the C face of a 4H-SiC seed crystal, with the growth temperature ranging from 2100 to 2300 °C and the growth pressure ranging from 1 to 10 mbar. High-purity nitrogen (N_2) gas was mixed into argon (Ar) gas with a volume fraction of 4% in the growth chamber to realize the N doping of 4H-SiC. The common slicing plane of (0001) or $(000\bar{1})$ only reflects the outcrops of TDs in 4H-SiC. In order to investigate the generation and evolution of TDs during the single-crystal growth of 4H-SiC, the 4H-SiC boule was then vertically sliced along the growth direction into nonpolar $(11\bar{2}0)$ wafers. The samples were mechanically polished by diamond abrasives to remove the wire-sawing-induced damages. Molten KOH etching at 550 °C for 10 min and subsequent photochemical etching in a 0.04 M KOH solution for 60 min were carried out to reveal dislocations and SFs on the $(11\bar{2}0)$ surfaces of 4H-SiC.[28] During the photochemical etching, SFs are referred to as quantum wells for highly efficient recombination of UV-generated electrons and holes.[29,30] Therefore, UV-generated holes can easily be trapped in the regions containing SFs during the photochemical etching process, rendering the imperfect regions a much lower etch rate than the neighboring host 4H-SiC crystal.

2.2. Characterizations. Surface morphologies of the etched 4H-SiC samples were examined by using the optical microscope (OM) (Olympus, BX53M), the atomic force microscope (AFM) (Bruker, Dimension XR), and the scanning electron microscope (SEM) (Carl Zeiss, Sigma 300). The polymorph of the sample was identified by a Raman scattering spectroscope (Horiba, LabRAM Odyssey) by employing a confocal optical microscope in the quasi-backscattering geometry at 532 nm used for excitation. Transmission electron microscopy specimens taken from the $(11\bar{2}0)$ surface of 4H-SiC were fabricated by using a focused ion beam microscope (Thermo Scientific, Helios 5 UX) with an energy of about 1 nA Ga^+ for final milling. Microstructure characterization was performed in a TEM (Thermo Scientific, Talos F200X) operated at 200 kV and a microscope (Thermo Scientific, Themis Z) equipped with a probe-side Cs corrector operated at 200 kV. Standard $\boldsymbol{g}\bullet\boldsymbol{b}$ analyses (where $\boldsymbol{g}$ is the diffraction vector and $\boldsymbol{b}$ is the Burgers vector) were performed to determine the Burgers vector of dislocations.[31] It is well known that GPA is a mathematical technique used in materials science to analyze the deformation and strain of crystalline solids,[32] which involves the analysis of reciprocal lattice vectors observed in high-resolution images. To obtain the atomic strain distribution around the defects and interfaces, GPA was calculated based on aberration-corrected high-resolution high-angle annular dark-field scanning TEM (HAADF-STEM) images, with the reciprocal lattice vectors of $(\bar{1}102)$ and $(0\bar{1}10)$ chosen for $[11\bar{2}0]$ zone axis-oriented samples.

3. RESULTS AND DISCUSSION

Figure 1a shows the OM image of the molten KOH etched $(11\bar{2}0)$ surface of 4H-SiC near the seed crystal. It is clear that oblate etch pits are formed after molten KOH etching. Combined with the height profile of a typical etch pit as shown in Figure 1b, we attribute the etch pits to the outcrops of the dislocation lines of TDs at the $(11\bar{2}0)$ surface.[33] Interestingly, the etch pits of TDs tend to line up along the $[1\bar{1}00]$ direction, which seems to be connected by linear patterns. In order to verify the issue, we perform photochemical etching on the molten KOH etched 4H-SiC samples. Photochemical etching is capable of revealing dislocations and SFs by removing the perfect 4H-SiC region.[28] Figure 1c,d displays the surface morphologies and height profiles of the 4H-SiC sample after subsequent molten KOH etching and photochemical etching. It is clear that photochemical etching reveals linear etch patterns on the $(11\bar{2}0)$ surface of the 4H-SiC sample, which would correspond to SFs or BPDs.

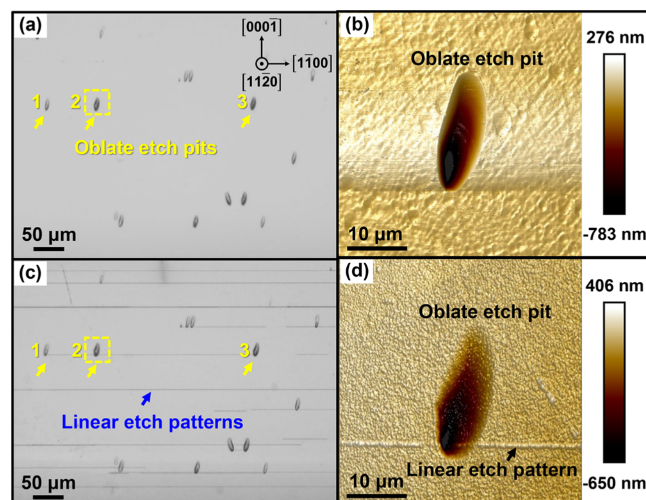

Figure 1. (a) Surface morphology of short oblate etch pits after molten KOH etching on the $(11\bar{2}0)$ surface in 4H-SiC. (b) Height profile of a representative oblate etch pit marked by the yellow dashed frame shown in panel (a). (c) Surface morphology after photochemical etching. (d) Height profile of a representative oblate etch pit marked by the yellow dashed frame shown in panel (c).

In order to determine the atomic structure of the linear etch patterns, a representative linear etch pattern is investigated by TEM. Figure 2a shows the dark-field image containing four linear etch patterns at weak-beam conditions with the diffraction vector of $(03\bar{3}0)$. According to the $\boldsymbol{g}\bullet\boldsymbol{b}$ analysis, the contrast is attributed to the basal plane SFs, which verifies the fact that photochemical etching reveals SFs on the $(11\bar{2}0)$ surface of 4H-SiC. Figure 2b shows the high-resolution HAADF-STEM image of a representative SF enclosed by the yellow dashed frame in Figure 2a. The stacking sequence of the perfect 4H-SiC region is (2, 2) in Zhdanov's notation, while the stacking sequence of the SF region is (3, 2).

To understand the underlying mechanism of the formation of TDs located at SFs (3, 2), we perform the GPA on the high-resolution HAADF-STEM image. According to the strain map as shown in Figure 2c, the strain distribution is in accordance with the interface between SF and the host 4H-SiC region. More importantly, the strain field is inhomogeneous along the SF, and the positions labeled by yellow arrows exhibit a

https://doi.org/10.1021/acs.cgd.3c00416
Cryst. Growth Des. 2023, 23, 5204−5210

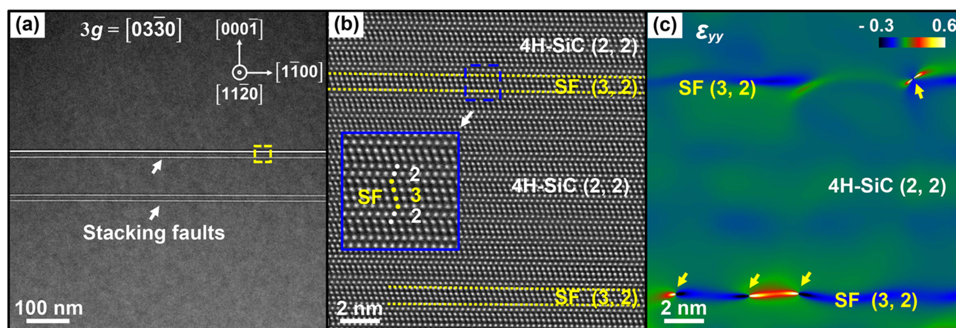

Figure 2. (a) Weak-beam dark-field image of the linear etch pattern with the diffraction vector of 3*g* = [03̄30]. (b) High-resolution HAADF-STEM image of SFs and host crystal taken from the area enclosed by the yellow dashed frame in panel (a). (c) Corresponding strain field of panel (b).

relatively higher strain (ε_{yy}) along the growth direction. Once the inhomogeneous stress along the SF exceeds the critical stress for the nucleation of TDs, the regions with higher stress at the SF/4H-SiC interface can serve as the nucleation sites for TDs. During N doping, N atoms tend to first substitute C atoms at the SFs because of the Suzuki effect.[34] This might give rise to the segregation of N dopants at the SFs and thus inhomogeneous strain distribution along the SF/4H-SiC interface.

Apart from the TD-related pits connected by SFs along the [11̄00] direction, macro-elevations extending along the [11̄00] direction with a height of 1−3 μm are also observed near the interface between the 4H-SiC seed crystal and the grown single-crystal boule. Figure 3a displays the SEM image of a

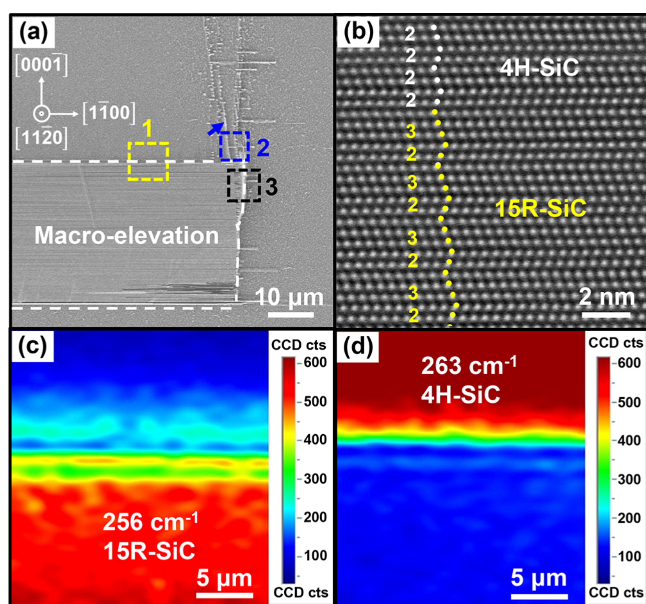

Figure 3. (a) SEM image of a macro-elevation enclosed by the white dashed frame. (b) High-resolution HAADF-STEM image of the macro-elevation. Intensity mappings of the Raman peaks at (c) 256 cm^{-1} and (d) 263 cm^{-1} of the region enclosed by the yellow dashed frame in panel (a).

typical macro-elevation after photochemical etching. It is found that the macro-elevation is composed of a bunch of SFs. Atomic-scale observations of the macro-elevation indicate that the stacking sequence of the Si−C bilayers is (3, 2) in Zhdanov's notation (Figure 3b). This indicates that the polymorph of the macro-elevation is 15R-SiC.[3] In order to verify the formation of 15R-SiC, we investigate micro-Raman spectroscopy of the region denoted by the yellow dashed frame in Figure 3a. Because the folded mode of the transverse acoustic (FTA) branch of 4H-SiC and 15R-SiC is located at 263 and 256 cm^{-1}, respectively,[35] we perform micro-Raman intensity mapping of the FTA branch of the region. As shown in Figure 3c,d, the micro-Raman intensities at the peak positions of 256 and 263 cm^{-1} are the highest in the off-macro-elevation and the macro-elevation region, respectively. This verifies that the polymorphs of the macro-elevation region and the host region correspond to 15R-SiC and 4H-SiC, respectively.

In addition, several elevated vertical etched lines along the growth direction of the *c*-axis direction are observed at the edge of the macro-elevation region. TEM observations are then applied to investigate the microstructure of the vertical lines in region 2 highlighted by the blue dashed frame in Figure 3a. Figure 4a,b shows the two-beam dark-field TEM images of region 2 with the diffraction vectors of *g* = [11̄00] and [0004], respectively. The contrast of dislocations in TEM images is determined by the scalar product ***g*•*b***, where *g* and *b* are the diffraction vector and the Burgers vector, respectively.[31] With the diffraction vectors of *g* = [11̄00], the dislocation lines of the vertical lines and BPDs lying on the basal plane are visible. BPDs with dislocation line directions of [112̄0] and [11̄00] are marked by the white dashed circles and white arrows (Figure 4a), respectively. We note that there exist two kinds of BPDs. The direction of the dislocation lines of BPDs indicated by the white dashed circles and white arrows is along the [12̄10] and [12̄10] or [2̄110] direction, respectively. However, the contrast of the vertical lines disappears with the diffraction vector of *g* = [0004], indicating that the Burgers vector of the vertical dislocations is perpendicular to [0004]. Combined with the fact that the dislocation lines of the vertical etched lines are orientated along the *c*-axis direction, the vertical line defects would correspond to TEDs with the Burger vector of [12̄10]a/3. We note that the zone axis of the left region (L) of the TEM sample (Figure 4a) is slightly inclined to the one in the middle region (M), which is confirmed by the corresponding diffraction patterns. It has been found that the LAGB can be regarded as dislocation walls of TEDs in 4H-SiC crystals.[36] Therefore, the vertical etched lines at the edge of the macro-elevation region can be attributed to LAGBs formed at the interface between 4H-SiC and 15R-SiC during the early stage of PVT growth.

In order to explore the generation mechanism of TEDs at the interface between 15R-SiC and 4H-SiC, we investigate the microstructure and strain distribution around the interface of

https://doi.org/10.1021/acs.cgd.3c00416
Cryst. Growth Des. 2023, 23, 5204−5210

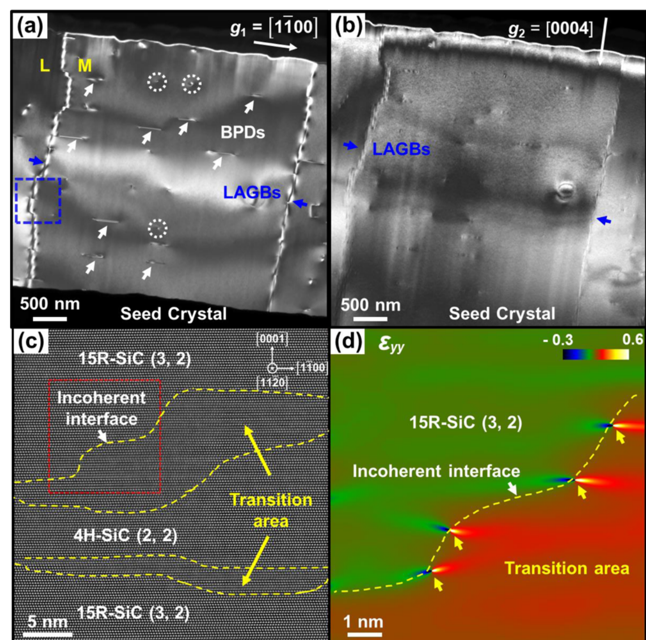

Figure 4. Two-beam dark-field TEM images of region 2 as highlighted by the blue dashed frame in Figure 3a with the diffraction vectors of (a) $\boldsymbol{g}$ = [1$\bar{1}$00] and (b) $\boldsymbol{g}$ = [0004], respectively. (c) High-resolution HAADF-STEM image of the interface between 15R-SiC and 4H-SiC, taken from region 3 enclosed by the blue dashed frame in Figure 3a, the transition areas are denoted by the yellow dashed lines. (d) Corresponding strain map of the incoherent interface taken from the area enclosed by the blue dashed frame in panel (c).

region 3 enclosed by the black dashed frame in Figure 3a. Figure 4c shows the atomic structure of the interface between 15R-SiC and 4H-SiC. The flat interface observed in SEM (Figure 3a) changes into curved configuration at the atomic scale. It is clear that a 4H-SiC lamellar is inserted in two neighboring 15R-SiC polymorphs due to the unstable growth condition at the early growth stage of 4H-SiC. Similar to the twinning partial dislocation slip on successive (111) planes in face-centered cubic Cu-based alloys,[37] the growth velocity of the polymorphs on successive (0001) basal planes along the [1$\bar{1}$00] direction is also different. This gives rise to the different scopes of 15R-SiC and 4H-SiC lamellae and thus the curved interface of 15R-SiC and 4H-SiC, which are indicated by the yellow dashed lines in Figure 4c. Compared with the neighboring structure of 15R-SiC and 4H-SiC, the lattice structure in the transition area is slightly out of order, and the corresponding contrast is a little blurred than the 15R-SiC and 4H-SiC matrix.

To reveal the strain distribution around the incoherent interface between 15R-SiC and 4H-SiC, GPA is carried out on the area enclosed by the red dashed frame as shown in Figure 4c. The atomic structure of the 15R-/4H-SiC interface demonstrates that there do not exist any extra or missing (0001) basal planes near the interface, which means that the lattice misfit and strain on the basal plane are negligible. Hence, only the strain along the growth direction ($\boldsymbol{\varepsilon}_{yy}$) is considered. The corresponding strain map shown in Figure 4d depicts the strain distribution on the incoherent interface between 15R- and 4H-SiC, indicating that the misfit stress is inhomogeneous around the 15R-/4H-SiC interface. The generation of TEDs is then motivated to release the misfit stress during the initial stage of the PVT growth process.

Besides the formations of TEDs (or LAGBs) at the interface between 15R- and 4H-SiC, it is found that the segments of the left LAGB as shown in Figure 4a are significantly kinked. One LAGB segment enclosed by the blue dashed frame is enlarged in Figure 5a. The results demonstrate that the LAGB is dislocation bundle comprised of multiple TEDs rather than individual dislocations, and the TEDs are regularly arrayed along the growth direction with a spacing distance of about 38 nm. Interaction with BPDs lying on the basal planes affects the configuration and defect behaviors of TEDs or LAGBs in the 4H-SiC boule. As seen from the configuration of the LAGB segments, it is found that the kink of the LAGB is caused by the interaction between the LAGB and BPDs. We note that the darker fringes in Figure 5a are related to surface damage introduced by Ga^+ beam during TEM sample preparation by using the FIB method. Figure 5b illustrates the interaction process of a TED with a BPD and thus the kinked configuration of the TED. As shown in Figure 5b, the TED and BPD have the same Burgers vector of $\boldsymbol{b}$ = a/3[1$\bar{2}$10], and the interaction of a TED (line XY) with a BPD (line AB) gives rise to two kinks QQ′ and PP′ lying on the basal plane (P_{AB}) in the TED and BPD,[38] respectively. For the LAGB consisting of TED bundles, the interaction between the TEDs and a BPD gives rise to the kink of the LAGB. The kink of BPD (PP′) is invisible because the BPD is still straight when projecting along the [11$\bar{2}$0] direction.

At last, we discuss the formation of TDs and LAGBs induced by SFs and 15R-SiC polymorphs at the early stage of PVT-grown 4H-SiC single crystals. It is known that the stacking fault energy of 4H-SiC is as low as 14.7 ± 2.5 $mJ \cdot m^{-2}$,[39] which gives rise to the formation of SFs in 4H-SiC. As illustrated in

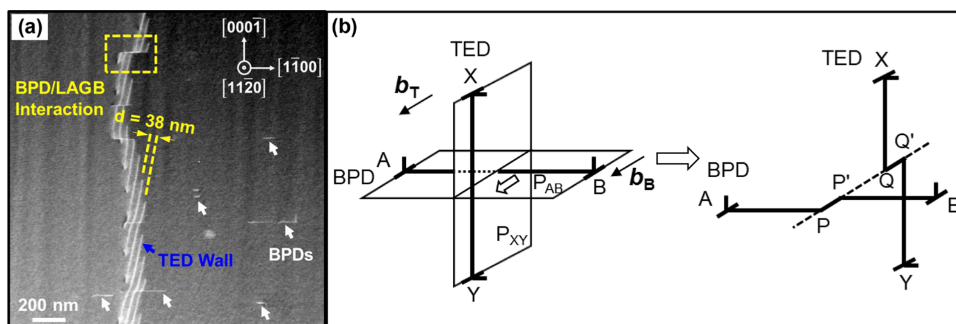

Figure 5. (a) HAADF-STEM image of one LAGB segment indicated by the blue dashed frame in Figure 4a. (b) Schematic illustration of interaction between a TED and a BPD with the same Burgers vector, with two kinks QQ′ and PP′ left lying on the basal plane in 4H-SiC.

https://doi.org/10.1021/acs.cgd.3c00416
Cryst. Growth Des. 2023, 23, 5204−5210

Figure 6, at the early stage of PVT growth, the high density of SFs is generated due to the nonstable spiral growth, as well as

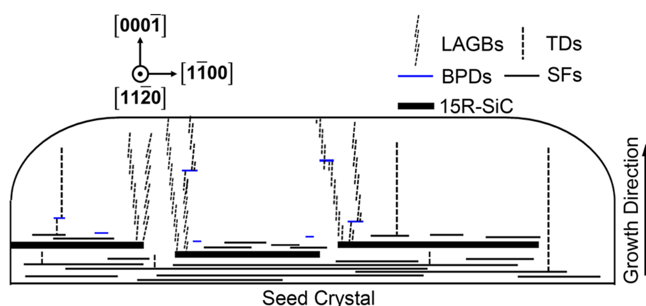

Figure 6. Schematic illustrations of TD generations associated with SFs and 15R-SiC polymorphs at the early growth stage of 4H-SiC.

the misfit stress between the interface between the seed crystal and the as-grown 4H-SiC single crystal. TEM observations indicate that the stacking sequence of the Si−C bilayers of the generated SFs is (3, 2) in Zhdanov's notation. GPA verifies that the strain distribution at the interface between (2, 2) and (3, 2) regions is inhomogeneous. Once the stress along the SF (3, 2) exceeds the critical stress of the formation of TDs, TDs located at the SF (3, 2) are formed. As the PVT growth proceeds, more SFs (3, 2) are generated. The high density of SFs (3, 2) initiates the polymorph fluctuation, which causes the formation of 15R-SiC. Similarly, the strain field distribution at the interface between 15R-SiC and 4H-SiC is also inhomogeneous. The high stress causes the formation of LAGB, which consists of a bunch of TEDs. Detailed TEM observations show that LAGBs in 4H-SiC single crystals can be kinked by the interaction between the TEDs constituting the LAGB and a BPD, rather than being straight along the growth direction of the 4H-SiC crystal. After the misfit stress between 15R-SiC and 4H-SiC is released by the formation and propagation of LAGBs and TDs, the single-crystal growth of 4H-SiC is stabilized.

4. CONCLUSIONS

In conclusion, we have revealed the generation mechanism of 15R-SiC, as well as the generation mechanism of TDs by SFs and 15R-SiC at the early growth stage of PVT-grown 4H-SiC single crystals with the assistance of defect-selective chemical etching and microstructure analyses. By combining molten KOH etching and photochemical etching of the $(11\bar{2}0)$ surface of 4H-SiC, we successfully revealed TD-related pits located at SF (3, 2)-related linear etch patterns, as well as LAGB-related etched lines at the interface between 15R-SiC and 4H-SiC. Detailed GPA has indicated that the strain field distribution along the SF (3, 2) is inhomogeneous, which gives rise to the formation of TDs located at SFs (3, 2). As the PVT growth proceeds, the accumulation of high density of SFs (3, 2) gives rise to the formation of 15R-SiC. Similarly, we have found that the strain field along the interface between 15R-SiC and 4H-SiC is inhomogeneous, which initiates the formation of LAGBs. The LAGBs in 4H-SiC are found to be capable of being kinked by the interaction between the TEDs constituting the LAGB and a BPD. Our work provides a clue for the reduction of dislocation density in the PVT-grown 4H-SiC single crystals.

■ ASSOCIATED CONTENT

Data Availability Statement

The data that support the findings of this study are available from the corresponding authors upon reasonable request.

■ AUTHOR INFORMATION

Corresponding Authors

Xiaodong Pi − *State Key Laboratory of Silicon and Advanced Semiconductor Materials & School of Materials Science and Engineering, Zhejiang University, Hangzhou, Zhejiang 310027, China; Institute of Advanced Semiconductors & Zhejiang Provincial Key Laboratory of Power Semiconductor Materials and Devices, Hangzhou Innovation Center, Zhejiang University, Hangzhou, Zhejiang 311200, China;* orcid.org/0000-0002-4233-6181; Email: xdpi@zju.edu.cn

Rong Wang − *State Key Laboratory of Silicon and Advanced Semiconductor Materials & School of Materials Science and Engineering, Zhejiang University, Hangzhou, Zhejiang 310027, China; Institute of Advanced Semiconductors & Zhejiang Provincial Key Laboratory of Power Semiconductor Materials and Devices, Hangzhou Innovation Center, Zhejiang University, Hangzhou, Zhejiang 311200, China;* orcid.org/0000-0003-3333-0180; Email: rong_wang@zju.edu.cn

Authors

Qinqin Shao − *State Key Laboratory of Silicon and Advanced Semiconductor Materials & School of Materials Science and Engineering, Zhejiang University, Hangzhou, Zhejiang 310027, China; Institute of Advanced Semiconductors & Zhejiang Provincial Key Laboratory of Power Semiconductor Materials and Devices, Hangzhou Innovation Center, Zhejiang University, Hangzhou, Zhejiang 311200, China*

Wenhao Geng − *State Key Laboratory of Silicon and Advanced Semiconductor Materials & School of Materials Science and Engineering, Zhejiang University, Hangzhou, Zhejiang 310027, China; Institute of Advanced Semiconductors & Zhejiang Provincial Key Laboratory of Power Semiconductor Materials and Devices, Hangzhou Innovation Center, Zhejiang University, Hangzhou, Zhejiang 311200, China*

Suocheng Xu − *Key Laboratory of Optical Field Manipulation of Zhejiang Province, Department of Physics, Zhejiang Sci-Tech University, Hangzhou 310018, China; IV-Semitec Co., Ltd., Hangzhou 311200, China*

Penglei Chen − *IV-Semitec Co., Ltd., Hangzhou 311200, China*

Xi Zhang − *Institute of Advanced Semiconductors & Zhejiang Provincial Key Laboratory of Power Semiconductor Materials and Devices, Hangzhou Innovation Center, Zhejiang University, Hangzhou, Zhejiang 311200, China*

Ruohan Shen − *School of Intelligent Manufacturing, Huzhou College, Huzhou 313000, China*

He Tian − *Institute of Advanced Semiconductors & Zhejiang Provincial Key Laboratory of Power Semiconductor Materials and Devices, Hangzhou Innovation Center, Zhejiang University, Hangzhou, Zhejiang 311200, China;* orcid.org/0000-0003-2108-3100

Deren Yang − *State Key Laboratory of Silicon and Advanced Semiconductor Materials & School of Materials Science and Engineering, Zhejiang University, Hangzhou, Zhejiang 310027, China; Institute of Advanced Semiconductors &*

https://doi.org/10.1021/acs.cgd.3c00416
Cryst. Growth Des. 2023, 23, 5204−5210

Zhejiang Provincial Key Laboratory of Power Semiconductor Materials and Devices, Hangzhou Innovation Center, Zhejiang University, Hangzhou, Zhejiang 311200, China

Complete contact information is available at:
https://pubs.acs.org/10.1021/acs.cgd.3c00416

Author Contributions

[#]Q.S. and W.G. contributed equally to this work.

Notes

The authors declare no competing financial interest.

ACKNOWLEDGMENTS

This work was supported by the National Natural Science Foundation of China (Grant Nos. 62274143, U22A2075, 12204161), "Pioneer" and "Leading Goose" R&D Program of Zhejiang (Grant Nos. 2022C01021, 2023C01010), National Key Research and Development Program of China (Grant No. 2018YFB2200101), Fundamental Research Funds for the Central Universities (Grant No. 2018XZZX003-02), and Natural Science Foundation of China for Innovative Research Groups (Grant No. 61721005).

REFERENCES

(1) Matsunami, H. Technological Breakthroughs in Growth Control of Silicon Carbide for High Power Electronic Devices. *Jpn. J. Appl. Phys.* **2004**, *43*, 6835−6847.

(2) Kimoto, T. Bulk and Epitaxial Growth of Silicon Carbide. *Prog. Cryst. Growth Charact. Mater.* **2016**, *62*, 329−351.

(3) Tsunenobu, K.; Cooper, J. A., *Fundamentals of Silicon Carbide Technology: Growth, Characterization, Devices and Applications*; Wiley, 2014.

(4) Kimoto, T.; Watanabe, H. Defect Engineering in SiC Technology for High-Voltage Power Devices. *Appl. Phys. Express* **2020**, *13*, 120101.

(5) Zhang, J.; Liang, T.; Lu, Y.; Xu, B.; Deng, T.; Zhang, Y.; Zeng, Z.; Pi, X.; Yang, D.; Wang, R. Effect of Hexagonality on the Pressure-Dependent Lattice Dynamics of 4H-SiC. *New J. Phys.* **2022**, *24*, 113015.

(6) Hobgood, H.; Brady, M. F.; Brixius, W. H.; Fechko, G.; Glass, R. C.; Henshall, D.; Jenny, J. R.; Leonard, R. T.; Malta, D. P.; Müller, S. G.; Tsvetkov, V. F.; Carter, J.; Calvin, H. Status of Large Diameter SiC Crystal Growth for Electronic and Optical Applications. *Mater. Sci. Forum* **2000**, *338−342*, 3−8.

(7) Tokuda, Y.; Yamashita, T.; Kamata, I.; Naijo, T.; Miyazawa, T.; Hayashi, S.; Hoshino, N.; Kato, T.; Okumura, H.; Kimoto, T.; Tsuchida, H. Structural Analysis of Double-Layer Shockley Stacking Faults Formed in Heavily-Nitrogen-Doped 4H-SiC During Annealing. *J. Appl. Phys.* **2017**, *122*, 045707.

(8) Wang, R.; Huang, Y. C.; Yang, D. R.; Pi, X. D. Impurities and Defects in 4H Silicon Carbide. *Appl. Phys. Lett.* **2023**, *122*, 180501.

(9) Gao, W.; Yang, G.; Qian, Y.; Han, X.; Cui, C.; Pi, X.; Yang, D.; Wang, R. Dislocation-Related Leakage-Current Paths of 4H Silicon Carbide. *Front. Mater.* **2022**, *10*, 1022878.

(10) Konishi, K.; Nakamura, Y.; Nagae, A.; Kawabata, N.; Tanaka, T.; Tomita, N.; Watanabe, H.; Tomohisa, S.; Miura, N. Direct Observation and Three Dimensional Structural Analysis for Threading Mixed Dislocation Inducing Current Leakage in 4H-SiC IGBT. *Jpn. J. Appl. Phys.* **2020**, *59*, 011001.

(11) Fujiwara, H.; Naruoka, H.; Konishi, M.; Hamada, K.; Katsuno, T.; Ishikawa, T.; Watanabe, Y.; Endo, T. Relationship between Threading Dislocation and Leakage Current in 4H-SiC Diodes. *Appl. Phys. Lett.* **2012**, *100*, 242102.

(12) Onda, S.; Watanabe, H.; Kito, Y.; Kondo, H.; Uehigashi, H.; Hosokawa, N.; Hisada, Y.; Shiraishi, K.; Saka, H. Transmission Electron Microscope Study of a Threading Dislocation with $\boldsymbol{b}$ = [0001] + <1$\bar{1}$00> and Its Effect on Leakage in a 4H-SiC MOSFET. *Philos. Mag. Lett.* **2013**, *93*, 439−447.

(13) Skowronski, M.; Ha, S. Degradation of Hexagonal Silicon-Carbide-Based Bipolar Devices. *J. Appl. Phys.* **2006**, *99*, 011101.

(14) Chung, S.; Wheeler, V.; Myers-Ward, R.; Eddy, C. R.; Gaskill, D. K.; Wu, P.; Picard, Y. N.; Skowronski, M. Direct Observation of Basal-Plane to Threading-Edge Dislocation Conversion in 4H-SiC Epitaxy. *J. Appl. Phys.* **2011**, *109*, 094906.

(15) Mina, A.; Song, H. Z.; Tangali, S. S.; Picard, Y. N. Glide of Threading Edge Dislocations after Basal Plane Dislocation Conversion During 4H-SiC Epitaxial Growth. *J. Cryst. Growth* **2015**, *418*, 7−14.

(16) Li, J.; Yang, G.; Liu, X.; Luo, H.; Xu, L.; Zhang, Y.; Cui, C.; Pi, X.; Yang, D.; Wang, R. Dislocations in 4H Silicon Carbide. *J. Phys. D: Appl. Phys.* **2022**, *55*, 463001.

(17) Yang, G.; Luo, H.; Li, J. J.; Shao, Q. Q.; Wang, Y. Z.; Zhu, R. Z.; Zhang, X.; Song, L. H.; Zhang, Y. Q.; Xu, L. B.; Cui, C.; Pi, X. D.; Yang, D. R.; Wang, R. Discrimination of Dislocations in 4H-SiC by Inclination Angles of Molten-Alkali Etched Pits. *J. Semicond.* **2022**, *43*, 122801.

(18) Shinagawa, N.; Izawa, T.; Manabe, M.; Yamochi, T.; Ohtani, N. Populations and Propagation Behaviors of Pure and Mixed Threading Screw Dislocations in Physical Vapor Transport Grown 4H-SiC Crystals Investigated Using X-Ray Topography. *Jpn. J. Appl. Phys.* **2020**, *59*, 091002.

(19) Hoshino, N.; Kamata, I.; Tokuda, Y.; Makino, E.; Kanda, T.; Sugiyama, N.; Kuno, H.; Kojima, J.; Tsuchida, H. Fast Growth of N-Type 4H-SiC Bulk Crystal by Gas-Source Method. *J. Cryst. Growth* **2017**, *478*, 9−16.

(20) Kamata, I.; Tsuchida, H.; Jikimoto, T.; Izumi, K. Structural Transformation of Screw Dislocations Via Thick 4H-SiC Epitaxial Growth. *Jpn. J. Appl. Phys.* **2000**, *39*, 6496.

(21) Dudley, M.; Huang, X. R.; Huang, W.; Powell, A.; Wang, S.; Neudeck, P.; Skowronski, M. The Mechanism of Micropipe Nucleation at Inclusions in Silicon Carbide. *Appl. Phys. Lett.* **1999**, *75*, 784−786.

(22) Sanchez, E. K.; Liu, J. Q.; De Graef, M.; Skowronski, M.; Vetter, W. M.; Dudley, M. Nucleation of Threading Dislocations in Sublimation Grown Silicon Carbide. *J. Appl. Phys.* **2002**, *91*, 1143−1148.

(23) Ha, S.; Nuhfer, N. T.; Rohrer, G. S.; Graef, M.; Skowronski, M. Origin of Domain Structure in Hexagonal SiC Boules Grown by the Physical Vapor Transport Method. *J. Cryst. Growth* **2000**, *220*, 308−315.

(24) Ha, S.; Nuhfer, N. T.; Rohrer, G. S.; de Graef, M.; Skowronski, M. Identification of Prismatic Slip Bands in 4H SiC Boules Grown by Physical Vapor Transport. *J. Electron. Mater.* **2000**, *29*, L5−L8.

(25) Heindl, J.; Strunk, H. P.; Heydemann, V. D.; Pensl, G. Micropipes: Hollow Tubes in Silicon Carbide. *Phys. Status Solidi A* **1997**, *162*, 251−262.

(26) Ohtani, N.; Katsuno, M.; Tsuge, H.; Fujimoto, T.; Nakabayashi, M.; Yashiro, H.; Sawamura, M.; Aigo, T.; Hoshino, T. Dislocation Processes During SiC Bulk Crystal Growth. *Microelectron. Eng.* **2006**, *83*, 142−145.

(27) Ohtani, N.; Katsuno, M.; Tsuge, H.; Fujimoto, T.; Nakabayashi, M.; Yashiro, H.; Sawamura, M.; Aigo, T.; Hoshino, T. Propagation Behavior of Threading Dislocations During Physical Vapor Transport Growth of Silicon Carbide (SiC) Single Crystals. *J. Cryst. Growth* **2006**, *286*, 55−60.

(28) Geng, W. H.; Guang, Y.; Zhang, X. Q.; Zhang, X.; Wang, Y. Z.; Song, L. H.; Chen, P. L.; Zhang, Y. Q.; Pi, X. D.; Yang, D. R.; Wang, R. Identification of Subsurface Damage of 4H-SiC Wafers by Combining Photo-Chemical Etching and Molten-Alkali Etching. *J. Semicond.* **2022**, *43*, 102801.

(29) Dorp, D. H.; Weyher, J. L.; Kelly, J. J. Anodic Etching of SiC in Alkaline Solutions. *J. Micromech. Microeng.* **2007**, *17*, S50.

(30) Weyher, J. L.; Lazar, S.; Borysiuk, J.; Pernot, J. Defect-Selective Etching of SiC. *Phys. Status solidi (a)* **2005**, *202*, 578−583.

(31) Liu, B. Y.; Liu, F.; Yang, N.; Zhai, X. B.; Zhang, L.; Yang, Y.; Li, B.; Li, J.; Ma, E.; Nie, J. F.; Shan, Z. W. Large Plasticity in Magnesium Mediated by Pyramidal Dislocations. *Science* **2019**, *365*, 73.

(32) Hÿtch, M.; Snoeck, E.; Kilaas, R. Quantitative Measurement of Displacement and Strain Fields from HREM Micrographs. *Ultramicroscopy* **1998**, *74*, 131−146.

(33) Yao, Y.; et al. Cross-Sectional Observation of Stacking Faults in 4H-SiC by KOH Etching on Nonpolar $\{1\bar{1}00\}$ Face, Cathodoluminescence Imaging, and Transmission Electron Microscopy. *Jpn. J. Appl. Phys.* **2014**, *53*, 081301.

(34) Kaneko, Y.; Kaneko, K.; Nohara, A.; Saka, H. Evidence for Suzuki Effect in an Fe-Ni-Cr Austenitic Stainless Steel. *Philos. Mag. A* **1995**, *71*, 399.

(35) Shimada, K.; Asada, K.; Yodo, M.; Ohtani, N. Raman Scattering Microscopy Imaging of Basal Plane Stacking Faults and Associated Partial Dislocations in 4H-SiC Crystals. *J. Appl. Phys.* **2020**, *127*, 165704.

(36) Ohtani, N.; Katsuno, M.; Tsuge, H.; Fujimoto, T.; Nakabayashi, M.; Yashiro, H.; Sawamura, M.; Aigo, T.; Hoshino, T. Behavior of Basal Plane Dislocations in Hexagonal Silicon Carbide Single Crystals Grown by Physical Vapor Transport. *Jpn. J. Appl. Phys.* **2006**, *45*, 1738.

(37) Zhu, Y. T.; Liao, X. Z.; Wu, X. L. Deformation Twinning in Nanocrystalline Materials. *Prog. Mater. Sci.* **2012**, *57*, 1−62.

(38) Derek, H.; Bacon, D. J., *Introduction to Dislocations*, 5 Edition ed.: UK, 2011, 268.

(39) Hong, M. H.; Samant, A. V.; Pirouz, P. Stacking fault energy of 6H-SiC and 4H-SiC single crystals. *Philos. Mag. A* **2000**, *80*, 919.